Proceedings of the
47th IEEE Conference on Decision and Control
Cancun, Mexico, Dec. 9-11, 2008

WeC03.4

Model-based $\mathcal{L}_1$ Adaptive Control of Hysteresis in Smart Materials

Xiang Fan and Ralph Smith

Abstract— **Undesired hysteresis and constitutive nonlinearities are present to varying degrees in all smart material based transducers when they are driven at high levels. This motivates the development of adaptive inverse compensation techniques that can approximately linearize the transducer response and also are sufficiently efficient to accommodate model uncertainties and the error introduced by inexact inverse algorithms. In this paper, we employ the homogenized energy model for describing hysteresis, and we incorporate the corresponding inverse filter in $\mathcal{L}_1$ control design to develop a robust adaptive inverse control approach. Asymptotic tracking properties of the proposed algorithm are established, and for periodic reference trajectories, the parameter convergence behavior is characterized. Simulation results are provided to illustrate the effectiveness of the proposed algorithm.**

Index Terms— **Robust adaptive control, hysteresis model, inverse filter.**

I. INTRODUCTION

Smart materials and structures play an important role in improving performance capabilities of aerospace, automotive, biomedical, industrial systems. Their advantages arise from number of factors including multi-functionality, large force or strain generation, high frequency and broadband actuator capabilities, and the potential for minimal weight increase. The need for high power density devices that can operate over a broad frequency range with precise control continues to draw interest in transducer designs that employ smart materials. For a number of applications, transducers employ ferroelectric or ferromagnetic drive elements which, respectively, produce electric or magnetic field induced displacements and forces. However, the coupling of fields to mechanical deformation, which makes these materials effective transducers, also introduces hysteresis and constitutive nonlinearities due to domain mechanisms. The fact that the hysteresis and nonlinearities are rate-, stress-, and temperature-dependent complicate the challenge of high performance high acturacy control. Whereas these nonlinear effects can be minimized by restricting input field levels for certain applications, moderate to high input fields are typically necessary in high performance applications. This requires accommodating hysteresis and constitutive nonlinearities in the control design so that large strain and high force capabilities can be effectively utilized.

One can introduce the nonlinear and hysteretic behavior into the control design via either inverse filters, used to linearize the actuator response, or direct nonlinear compensation using nonlinear control designs. The use of inverse filters has the advantage of providing linear control designs and can improve tracking performance by effectively compensating for nonlinear and irreversible material behavior; however, these advantages are only realized if the constitutive model is efficient enough to be inverted in real time. This complexity can sometimes be avoided by the use of nonlinear control designs which circumvent the need for an inverse filter and determines the input signals that directly incorporate actuator nonlinearities. However this approach introduces challenges in identifying robust numerical algorithms that can achieve efficient convergence.

It is the first approach that we consider here where a model-based inverse compensator is directly incorporated into the control design. The key to constructing an inverse compensator which accommodate hysteretic behaviors is the development of material models that can be efficiently inverted. The present analysis employs the homogenized energy model due to its energy basis and flexibility with regard to numerous operating conditions. As detailed in [1], it has been demonstrated that its corresponding inversion can be achieved at reasonable accuracy and speed; Whereas such compensation is never exact due to discretization and modeling errors, the variability between inverse and hysteretic device can be viewed as a structural uncertainty which motivates consideration of the $\mathcal{L}_1$ control design.

II. MODEL DEVELOPMENT

The homogenized energy model employed in the present analysis incorporates mesoscopic material behavior at the domain with a stochastic homogenization framework to predict macroscopic material behavior. A distribution of interaction fields and coercive fields is implemented to model polarization switching processes that typically occur in the presence of material non homogeneities and residual fields. Boltzmann relations are employed to model thermal relaxation behavior when thermal energy affects polarization switching. Macroscopic material behavior is determined by homogenizing the local polarization variants according to the distribution of interaction and coercive fields.

A. Homogenized Energy Model

The equations governing the homogenized energy model are summarized here. A detailed review of the modeling framework is given in [4]. The homogenized energy model is based on an energy description at the mesoscopic

---

Supported in part by the Air Force Office of Scientific Research through the grant AFOSR-FA9550-04-1-0203 and AFOSR-FA9550-08-1-0348.

X. Fan is with the Center for Research in Scientific Computing, Department of Mathematics, North Carolina State University, Raleigh NC 27695 USA (`email: xfan2@ncsu.edu`)

R. Smith is with the Center for Research in Scientific Computing, Department of Mathematics, North Carolina State University, Raleigh NC 27695 USA (`email: rsmith@eos.ncsu.edu`)

978-1-4244-3124-3/08/$25.00 ©2008 IEEE

length scale. This local energy formulation is used to predict macroscopic behavior using a stochastic representation of material inhomogeneities.

In the absence of applied stresses σ, the Gibbs free energy for ferroelectric materials at the mesoscopic length scale is

$$G = \psi(P) - EP \tag{1}$$

where $\psi(P)$ is the Helmholtz energy approximated by the piecewise quadratic function

$$\psi(P) = \begin{cases} \eta(P+P_R)^2/2, & P \le -P_I \\ \dfrac{\eta}{2}(P_I - P_R)\left(\dfrac{P^2}{P_I} - P_R\right), & |P| < P_I \\ \eta(P-P_R)^2/2, & P \ge P_I. \end{cases} \tag{2}$$

Here E is the electric field, P is the polarization, P_I denotes the positive inflection point at which the switch occurs, P_R is the local remanence polarization and η is the reciprocal slope $\frac{\partial E}{\partial P}$. The one-dimensional Helmholtz energy function is double-well potential below the Curie point T_c which gives rise to a stable spontaneous polarization with equal magnitude in the positive and negative directions. More details can be found in [4].

The Boltzmann relation gives rise to the local expected values

$$\langle P_+ \rangle = \frac{\int_{P_I}^{\infty} \exp(-G(E+E_I,P)V/kT)dP}{\int_{P_I}^{\infty} P\exp(-G(E+E_I,P)V/kT)dP} \tag{3}$$

$$\langle P_- \rangle = \frac{\int_{-\infty}^{-P_I} \exp(-G(E+E_I,P)V/kT)dP}{\int_{\infty}^{-P_I} P\exp(-G(E+E_I,P)V/kT)dP} \tag{4}$$

of the polarization associated with positive and negatively oriented dipoles, respectively. Here V is the volume of the mesoscopic layer, k is Boltzmann's constant, and T is the temperature.

The local polarization variants are defined by a volume fraction of variants x_+ and x_- having positive and negative orientations, respectively. The relation $x_- + x_+ = 1$ must hold for the volume fraction of polarization variants.

The local average polarization is qualified by the relation

$$\overline{P} = x_+\langle P_+ \rangle + x_-\langle P_- \rangle. \tag{5}$$

The macroscopic polarization is computed from the distribution of local variants from the relation

$$\begin{aligned}[P(E)](t) = \;& \int_{-\infty}^{\infty}\int_0^{\infty} \nu_c(E_c)\nu_I(E_I) \\ & \cdot\overline{P}(E+E_I;E_c;x_+)dE_I dE_c\end{aligned} \tag{6}$$

Here $\nu(E_c)$ and $\nu(E_I)$ respectively denote the densities of coercive field value E_c (at which a dipole changes its orientations) and interaction field value E_I and x_+ represents the distribution of the local variants. The densities can often be modeled as lognormal or normal distributions. However, when more accurate model predictions are critical, a general density can be fit to data. As detailed in [4], the model for magnetic material is equivalent.

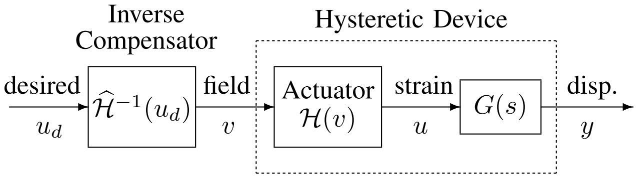

Fig. 1. Model-based inverse compensation.

B. Inverse Compensator

As discussed in Section I, one strategy for designing robust control laws for hysteretic actuators it to employ a model for describing hysteresis, and construct an inverse representation of the model which can be used as compensator before the the hysteretic actuator in the manner depicted in Fig. 1. The composite system to be controlled is then approximately linear and time-invariant. This allows robust control theories to be utilized, including the $\mathcal{L}_1$ control method employed here.

The inverse compensator we employ is the inverse of the homogenized energy model. To construct the inverse representation of (6), we need to determine the field level necessary to bring the actuator to the given value of polarization (or strain). More precisely, given any valid state x_+ and any $\widehat{P}$ within the operating range of the material, determine E such that $P = \widehat{P}$, where P is the solution of (6). Due to the nonlinearity and dependence on x_+, it is not feasible to invert (6) analytically. Thus, the problem is reformulated as a numerical root finding problem; namely, determining the value E such that for a given x_+ and $\widehat{P}$,

$$P(E;\, x_+) - \widehat{P} = 0. \tag{7}$$

Additional details are provided in [1].

III. MODEL-BASED $\mathcal{L}_1$ INVERSE CONTROL ARCHITECTURE

Consider the dynamic system:

$$\begin{aligned} \dot{\mathbf{x}}(t) &= \mathbf{A}\mathbf{x}(t) + \mathbf{b}u(t), \quad u(t) = [\mathcal{H}(v)](t) \\ y(t) &= \mathbf{c}^T\mathbf{x}(t) \end{aligned} \tag{8}$$

The matrix $\mathbf{A}$ may be unknown or uncertain and we assume that there exists a known and stable matrix $\mathbf{A}_m \in \mathbb{R}^{n\times n}$ and a vector of ideal parameter $\theta(t) \in \mathbb{R}^n$ such that $(\mathbf{A}_m, \mathbf{b})$ is controllable and $\mathbf{A} - \mathbf{A}_m = \mathbf{b}\,\theta^T$. We further assume the (unknown) parameter vector $\theta(t)$ belongs to a given compact convex set Θ. Here $u(t) = [\mathcal{H}(v)](t)$ is the driving force generated by the hysteretic actuator $\mathcal{H}$ where $v(t)$ is the input field to the actuator.

Next we incorporate the approximate inverse of homogenized energy model as the inverse compensator and use it before the actuator $\mathcal{H}$ (see Fig. 1). The driving force $u(t)$ can be rewritten as

$$u(t) = [\mathcal{H}(v)](t) = [\mathcal{H}\widehat{\mathcal{H}}^{-1}(u_d)](t) \tag{9}$$

where the signal $u_d(t)$ is used as the input of the inverse compensator $\widehat{\mathcal{H}}^{-1}(\cdot)$ to generate the control field $v(t)$ which is then applied to the hysteretic device.

Substituting (9) and $\mathbf{A} - \mathbf{A}_m = \mathbf{b}\theta^T$ into (8) yields

$$\begin{aligned} \dot{\mathbf{x}}(t) &= \mathbf{A}_m\mathbf{x}(t) + \mathbf{b}\Big([\mathcal{H}\widehat{\mathcal{H}}^{-1}(u_d)](t) + \theta^T\mathbf{x}(t)\Big), \\ y(t) &= \mathbf{c}^T\mathbf{x}(t). \end{aligned} \tag{10}$$

Our objective is to design a low-frequency adaptive controller $u_d(t)$ such that $y(t)$ tracks a given bounded reference signal $r(t)$ while all other error signals remain bounded.

While such model-based inverse compensation is never exact due to the discretization or modeling errors, the mismatch between inverse and hysteretic actuator can be designed to be small and thus be assumed bounded in magnitude; i.e.,

$$u(t) = u_d(t) + \sigma(t) \tag{11}$$

where $\sigma(t)$ is the inversion error and satisfies $|\sigma(t)| \leq \Delta_0 \in \mathbb{R}$. We can thus model the inversion error as an external time-varying disturbance and attenuate its impact by $\mathcal{L}_1$ control techniques [2].

The elements of the model-based $\mathcal{L}_1$ adaptive controller are introduced next.

We consider the output predictor

$$\begin{aligned} \dot{\hat{\mathbf{x}}}(t) &= \mathbf{A}_m\hat{\mathbf{x}}(t) + \mathbf{b}(u_d(t) + \hat{\theta}^T\mathbf{x}(t) + \hat{\sigma}(t)), \\ \hat{y}(t) &= \mathbf{c}^T\hat{\mathbf{x}}(t). \end{aligned} \tag{12}$$

which has a similar structure to the system in (10). The differences are: (i), the unknown parameter vector $\theta(t)$ is replaced by the adaptive estimate $\hat{\theta}(t)$, (ii), driving force $u(t) = [\mathcal{H}\widehat{\mathcal{H}}^{-1}(u_d)](t)$ is replaced by the relation (11) with inversion error estimate $\hat{\sigma}(t)$. Two estimates, $\hat{\theta}(t)$ and $\hat{\sigma}(t)$, are governed the projection-based adaptation laws

$$\begin{aligned} \dot{\hat{\theta}}(t) &= \Gamma_c \operatorname{Proj}\big[\hat{\theta}(t),\, -\mathbf{x}(t)\tilde{\mathbf{x}}^T(t)Pb\big], \quad \hat{\theta}(0) = \theta_0 \\ \dot{\hat{\sigma}}(t) &= \Gamma_c \operatorname{Proj}\big[\hat{\sigma}(t),\, -\tilde{\mathbf{x}}^T(t)Pb\big], \qquad \hat{\sigma}(0) = \sigma_0 \end{aligned} \tag{13}$$

where the signal $\tilde{\mathbf{x}}(t) = \hat{\mathbf{x}}(t) - \mathbf{x}(t)$ is the error between the states of the predictor and the physical system and P is the solution of the algebraic Lyapunov equation $\mathbf{A}_m^T P + P\mathbf{A}_m = -Q$, $Q > 0$. Projection operator $\operatorname{Proj}[\cdot,\cdot]$ is defined by

$$\operatorname{Proj}[p, x]|_i = \begin{cases} x_i, & \|p\| \leq M; \\ 0, & \text{otherwise.} \end{cases}$$

The $\mathcal{L}_1$ control method allows for the incorporation of a low-pass filter into the feedback-loop which passes lower-frequency signals and attenuates higher-frequency signals.

Letting $k_g = \frac{1}{\mathbf{c}^T\mathbf{A}_m^{-1}\mathbf{b}}$, the control signal $u_d(t)$ is generated through the low-pass system

$$u_d(s) = C(s)\big(k_g r(s) - \hat{\theta}^T(s)x(s) - \hat{\sigma}(s)\big) \tag{14}$$

where $C(s)$ is a pre-specified low-pass filter with low-pass gain $C(0) = 1$ and s is the Laplace variable.

With the low-pass filter C(s), the last two terms of the right hand side of (14) can be viewed as time-varying disturbances, which are not prevented from having high-frequency oscillations.

The complete $\mathcal{L}_1$ controller consists of (12)-(14) subject to the $\mathcal{L}_1$-*gain stability requirement:* design $C(s)$ to satisfy

$$\|\bar{G}(s)\|_{\mathcal{L}_1} L < 1, \qquad L = \max_{\theta\in\Theta} \sum_{i=1}^{n} |\theta_i(t)| \tag{15}$$

where $\overline{G}(s) = (s\mathbb{I} - \mathbf{A}_m)^{-1}b(1 - C(s))$, and the $\mathcal{L}_1$ gain for a stable proper m input n output transfer function, say $G(s)$, is defined as

$$\|G(s)\|_{\mathcal{L}_1} = \max_{i=1,\cdots,n} \left(\sum_{j=1}^{m} \int_0^\infty |g_{ij}(t)| dt \right).$$

Here $g_{ij}(t)$ is the impulse response of $G_{ij}(s)$, the i^{th} row j^{th} column element of $G(s)$.

For the specific choice of $C(s) = \dfrac{k}{s+k}$ and constant parameter vector $\theta(t)$, the state space form of the closed-loop reference system (12) and (14) is

$$\begin{aligned} \dot{\hat{\mathbf{x}}}(t) &= \mathbf{A}_m\hat{\mathbf{x}}(t) + \mathbf{b}(u_d(t) + \hat{\theta}^T\mathbf{x}(t) + \hat{\sigma}(t)), \\ \dot{u}_d(t) &= -ku_d(t) + k(k_g r(t) - \hat{\theta}^T(t)\mathbf{x}(t) - \hat{\sigma}(t)) \end{aligned}$$

The stability requirement can be simplified to choosing a gain k such that matrix

$$A_g = \begin{bmatrix} \mathbf{A}_m + \mathbf{b}\,\theta^T & \mathbf{b} \\ -k\theta^T & -k \end{bmatrix}$$

is stable for all $\theta \in \Theta$.

Note that when $C(s) = 1$ and with ideal parameter vector $\theta(t)$, u_d reduces to the ideal control signal

$$u_{id}(t) = k_g r(t) - \theta^T\mathbf{x}_{id} - \sigma(t) \tag{16}$$

and (16) is the one that leads to desired system response

$$\dot{\mathbf{x}}_{id}(t) = \mathbf{A}_m\mathbf{x}_{id}(t) + \mathbf{b}k_g r(t) \tag{17}$$

by canceling the uncertainties exactly. In the closed-loop predictor system (12)-(14), $u_{id}(t)$ is further low-pass filtered by $C(s)$ in (3.9) to have guaranteed low-frequency range. Thus, the system in (12)-(14) has a different response as compared to (17) achieved with (16). It has been proved in [2] that the response of the state predictor (12) can be made as close as possible to the response of the ideal system (17) by reducing $\|\overline{G}(s)\|_{\mathcal{L}_1}$ arbitrarily small, and $\|\overline{G}(s)\|_{\mathcal{L}_1}$ can be made arbitrarily small by appropriately choosing the design constants; further details may be found in [2] and [3].

IV. SIMULATION

A. Explicit Method

We first apply an explicit method (ode15s) to solve the ODE system (12)-(14).

Consider a single-frequency sinusoidal function $r(t) = \cos(t)$. Since the frequency of $r(t)$ is $1/2\pi$ Hz ($= 1$ rad/sec), based on the above analysis, this $r(t)$ could pass the filter and reference model unchanged. Theoretically, the tracking output $x_1(t)$ should exactly match the shape of $r(t) = \cos(t)$ after $x_1(t)$ converges. Simulation results are shown in Fig 2(a). We note that the system output $x_1(t)$ converges to $r(t)$ asymptotically whereas $x_1(t)$ lags behind the reference signal $r(t)$ with delay time of about $t_0 = 0.62$ sec. The system output $x_1(t)$ and predictor output $\hat{x}_1(t)$ are almost the same. To cancel out the delay, we could redefine $r(t)$ by $r(t + t_0)$, so it requires that we should have an exact prediction of the time-delay t_0 in advance. The performance for $r(t) = \cos(t)$ with time compensation is shown in Fig. 2(b), and we can see that the $x_1(t)$ could exactly track the reference signal $r(t)$ if we have a good prediction of the time delay. Next, we consider a multi-frequency sinusoidal reference signal $r(t) = 2\cos(t) + 10\cos(\pi t/5)$. We keep the same values for all other parameters. This multi-frequency $r(t)$ could also pass the filter and reference model unchanged. The simulation result shown in Fig. 3(a) points out that time-delay is independent of the frequencies of the reference signal $r(t)$; it only depends on the chosen predictor and controller (low-pass filter), while a rigorous relationship between the control structure and time delay has not been derived yet. The performance for $r(t) = 2\cos(t) + 10\cos(\pi t/5)$ with time compensation is shown in Fig. 3(b).

Further, two typical trajectories common to nanopositioning and industrial applications are plotted in Fig. 4. Simulation results for the trajectories $r_1(t)$ and $r_2(t)$ are plotted respectively in Fig. 5 and Fig. 6. The results illustrate that the $\mathcal{L}_1$ control design employing homogenized energy model based inverse filters can maintain a tracking accuracy once cutting commences even though the transducer is operating in the hysteretic and nonlinear regime.

B. Implicit Euler Method

Secondly we apply the implicit Euler method to solve the ODE system (12)-(14). Using the implicit Euler method, we aim to see if it can improve the time delay problem. The simulation results for the reference input $r = \cos(t)$ are shown in Fig. 7. We see that the tracking performance is much more stable compared to the results obtained by using ODE15s (see Fig. 2), but there is no significant improvement in reducing the time delay, and it takes 60% more CPU time. Next, we apply the implicit Euler method to the same multi-frequency reference signal that we used in Section A; i.e., $r(t) = 2\cos(t) + 10\cos(\pi t/5)$. We note that the results, shown in Figure 8, are quite similar to the results obtained using ode15s which means that, for this $r(t)$, the implicit method does not significantly improve the tracking performance, and it is more time consuming and costly.

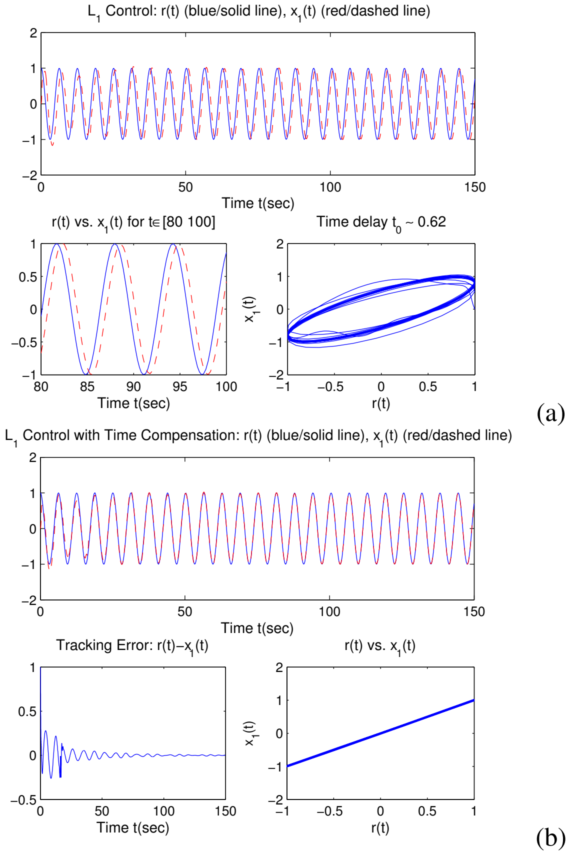

(a)

(b)

Fig. 2. Performance of the $\mathcal{L}_1$ adaptive controller for $r = \cos(t)$ with (a) no time compensation and (b) time compensation.

V. CONCLUDING REMARKS

In this paper, a robust control framework is developed by combining an inverse compensation with $\mathcal{L}_1$ control theory. The control design has focused on applications where the reference displacement is known in advance and precise control is desired at relatively high speeds. The incorporation of the homogenized energy model in the control design is shown to significantly improve the tracking performance. Simulations of an unstable non-minimum phase system verify the efficiency of the control framework. However, a

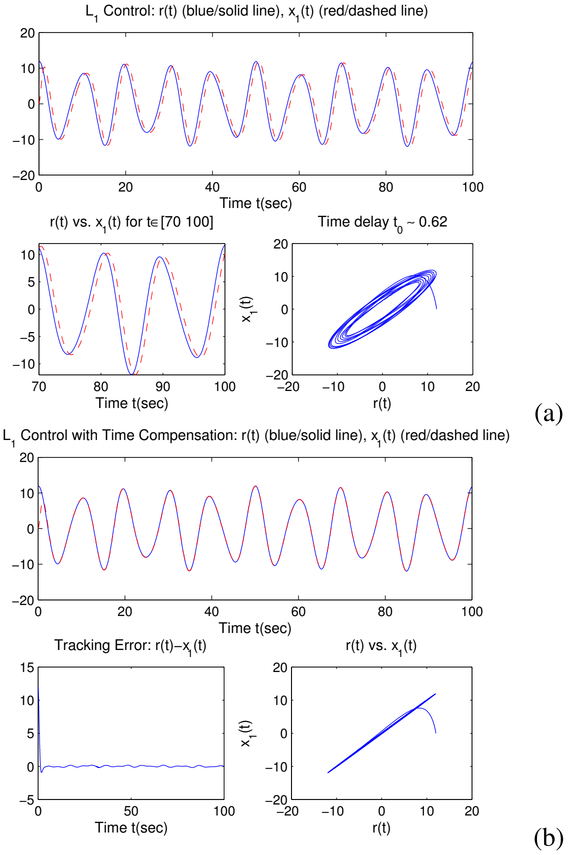

Fig. 3. Performance of the $\mathcal{L}_1$ adaptive controller for $r = 2\cos(t) + 10\cos(\pi t/5)$ with (a) no time compensation and (b) time compensation.

time-delay is observed in the performance of trackings. This motivates our next step to correlate the control structure with the time-delay.

REFERENCES

[1] T.R. Braun, R.C. Smith, "Efficient Implementation of Algorithms for Homogenized Energy Models", *Continuum Mechanics and Thermodynamics*, 18(3-4), pp.137-155, 2006.

[2] C. Cao, N. Hovakimyan, "Design and Analysis of a Novel $\mathcal{L}_1$ Adaptive Control Architecture with Guaranteed Transient Performance", *Proc. American Control Conference,* 2006.

[3] C. Cao, N. Hovakimyan, "$\mathcal{L}_1$ Adaptive Controller for System in the Presence of Unmodelled Actuator Dynamics", *Proc. 46th IEEE Conference on Decision and Control*, 2007.

[4] R.C. Smith, " Smart Material Systems: Model Development." Philadelphia, PA: SIAM, 2005.

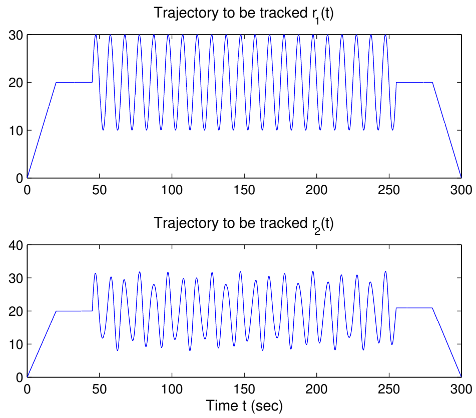

Fig. 4. Tracking trajectories that include a ramp, hold and periodic part.

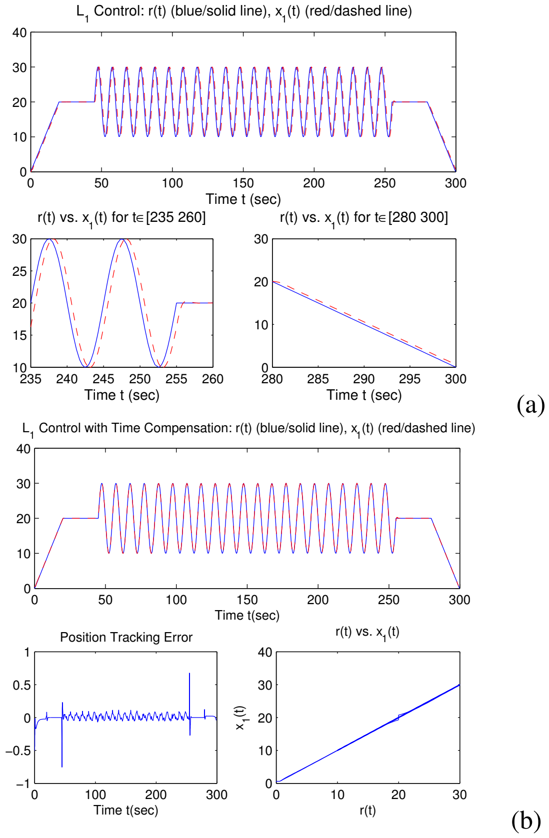

Fig. 5. Performance of $\mathcal{L}_1$ adaptive controller for $r_1(t)$ with (a) no time compensation and (b) time compensation.

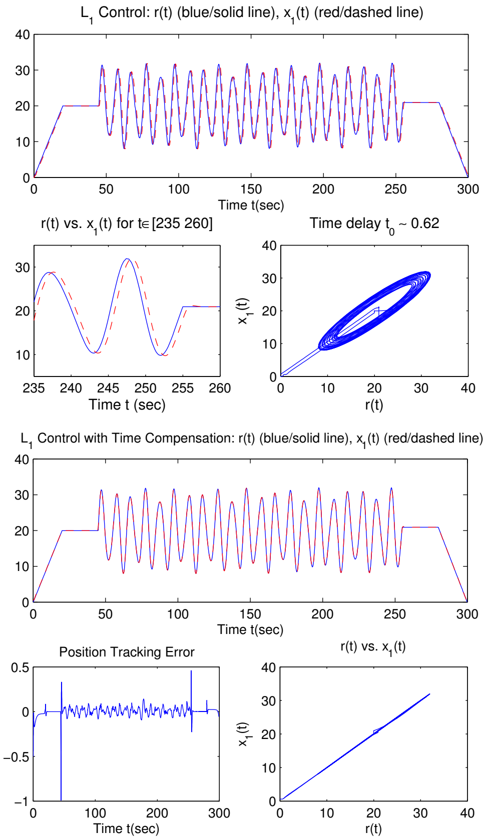

(a)

(b)

Fig. 6. Performance of $\mathcal{L}_1$ adaptive controller for $r_2(t)$ with (a) no time compensation and (b) time compensation.

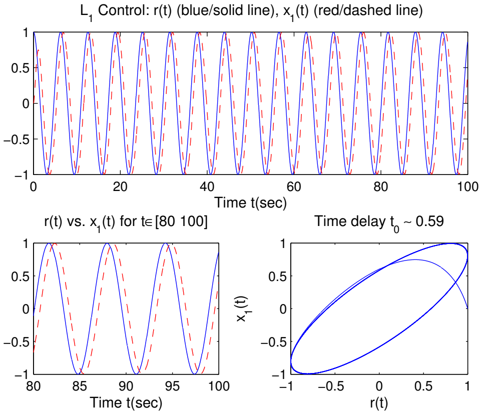

(a)

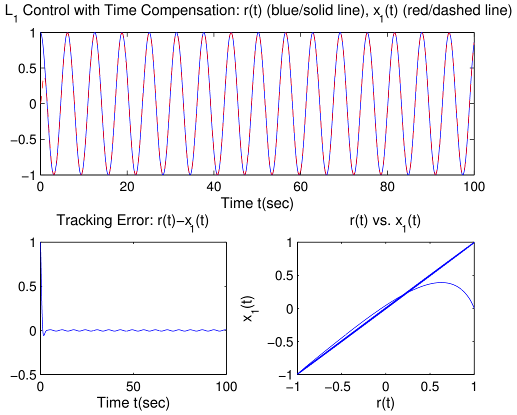

(b)

Fig. 7. Performance of the $\mathcal{L}_1$ adaptive controller for $r(t) = \cos(t)$ with the implicit Euler method with (a) no time compensation and (b) time compensation.

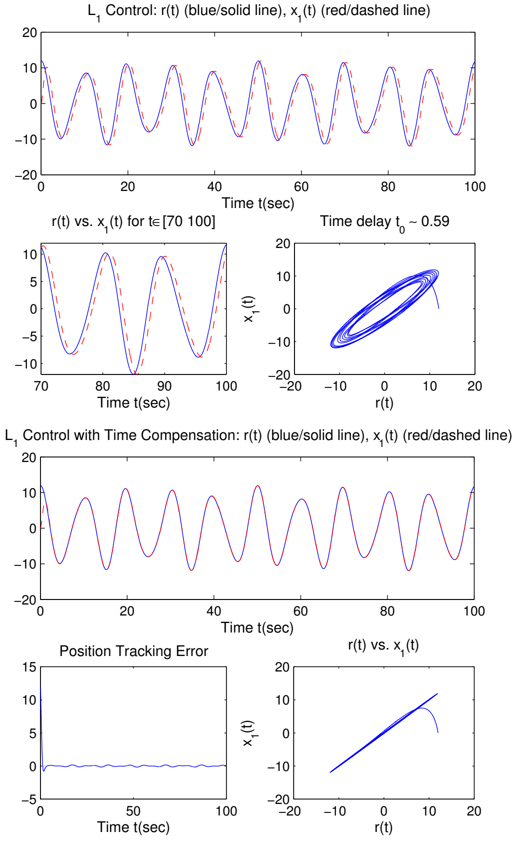

(a)

(b)

Fig. 8. Performance of the $\mathcal{L}_1$ adaptive controller for $r = 2\cos(t) + 10\cos(\pi t/5)$ with the implicit Euler method with (a) no time compensation and (b) time compensation.